inorganics

MDPI

Article

Dependency of Crystal Violet Dye Removal Behaviors onto Mesoporous V_2O_5-g-C_3N_4 Constructed by Simplistic Ultrasonic Method

Mohamed Ali Ben Aissa [1,*], Abueliz Modwi [1], Abuzar E. A. E. Albadri [2] and Sayed M. Saleh [2,3]

[1] Department of Chemistry, College of Science and Arts, Qassim University, Ar-Rass 51921, Saudi Arabia
[2] Department of Chemistry, College of Science, Qassim University, Buraidah 51452, Saudi Arabia
[3] Chemistry Branch, Department of science and mathematics, Faculty of Petroleum and Mining Engineering, Suez University, Suez 43721, Egypt
* Correspondence: m.benaissa@qu.edu.sa

Abstract: This research examined the production of a V_2O_5-g-C_3N_4 nanocomposite to remove organic dyes from wastewater. To generate the V_2O_5-g-C_3N_4 nanocomposite, the sonication method was applied. The testing of V_2O_5-g-C_3N_4 with various dyes (basic fuchsin (BF), malachite green (MG), crystal violet (CV), Congo red (CR), and methyl orange (MO)) revealed that the nanocomposite has a high adsorption ability towards BF, MG, CV, and CR dyes in comparison with MO dye. It was established that the modification of pH influenced the removal of CV by the V_2O_5-g-C_3N_4 nanocomposite and that under optimal operating conditions, efficiency of 664.65 mg g^{-1} could be attained. The best models for CV adsorption onto the V_2O_5-g-C_3N_4 nanocomposite were found to be those based on pseudo-second-order adsorption kinetics and the Langmuir isotherm. According to the FTIR analysis results, the CV adsorption mechanism was connected to π–π interactions and the hydrogen bond.

Keywords: V_2O_5-g-C_3N_4 nanocomposite; crystal violet adsorption; hydrogen bond; π–π interactions

Citation: Ben Aissa, M.A.; Modwi, A.; Albadri, A.E.A.E.; Saleh, S.M. Dependency of Crystal Violet Dye Removal Behaviors onto Mesoporous V_2O_5-g-C_3N_4 Constructed by Simplistic Ultrasonic Method. *Inorganics* **2023**, *11*, 146. https://doi.org/10.3390/inorganics11040146

Academic Editor: Eleonora Aneggi

Received: 4 March 2023
Revised: 24 March 2023
Accepted: 27 March 2023
Published: 30 March 2023

1. Introduction

With rapid industrialization, the environmental damage caused by organic dye wastewater is intensifying and becoming more severe. Organic dyes are commonly employed in cosmetics, food additives, paper-making, leather, and textile industries [1–3]. Consequently, substantial quantities of organic dyes are generated, and significant amounts of dyes are discharged into wastewater, which can cause highly hazardous byproducts in the environment [4–6]. Due to their aromatic character, organic dyes such as crystal violet (CV) include several functional groups that are persistent and difficult to decompose. CV is utilized in the manufacture of black and blue inks for ballpoint pens and printer ink jets [7,8]. CV is also used to produce waxes, leather, varnish, fertilizers, detergents, medications, and color paints [9–11]. However, CV, similar to most dyes, is a toxic carcinogenic with a recalcitrant classification because of its non-biodegradability, persistence in various environments, and nasty microbial metabolization [12–14]. Moreover, CV generates unpleasant colorations of water bodies, resulting in reduced light penetration for photosynthetic activities, negatively impacting aquatic life, such as the development of tumors in fish [10,15]. In order to ensure the life of aquatic organisms and humans, CV must be removed from wastewater before release.

Graphitic carbon nitride (g-C_3N_4), a 2D metal-free semiconductor, has acquired traction in energy storage and environmental applications, and as a photocatalyst for CO_2 reduction [16], hydrogen production [17], and contaminant degradation [18,19] due to its facile fabrication method, excellent thermal stability, low cost, and environmental friendliness [20–23]. Despite the plethora of research on g-C_3N_4 as a photocatalyst, there are only

a few papers on its adsorption uses [24–26]. Even though photocatalytic degradation can totally eliminate environmental contaminants, it is hampered by the formation of byproducts and relatively high running costs [27,28]. On the contrary, adsorption can remove significant quantities of contaminants without producing byproducts.

Due to its limited specific surface area (<10 m^2/g) and single surface functional group [29], pure g-C_3N_4 is not commonly employed in adsorption procedures [30]. Over the years, numerous modification techniques have been developed to increase the application of g-C_3N_4 [31–34]. In order to improve the removal efficiency of hazardous dyes, researchers have increasingly concentrated on modifying pure g-C_3N_4 by element doping, controlling its morphology, semiconductor recombination, and stripping [29]. Doping with heteroatoms is an excellent method for improving the adsorption of carbon-based compounds [33,35–39]. Vanadium pentoxide (V_2O_5), which possesses high oxidation ability, chemical inertness, and long-term stability against photochemical degradation, has been extensively utilized in numerous applications, including sensors, batteries, and catalysts [40–42].

We think this is the first study to successfully synthesize V_2O_5 incorporated with g-C_3N_4 with high surface area and efficient elimination of organic dyes, which opens up new avenues for the applications of g-C_3N_4 materials.

2. Results and Discussions

2.1. The V_2O_5-g-C_3N_4 Nanosorbent Characteristics

The morphologies and microstructures of the V_2O_5-g-C_3N_4 nanosorbent were further investigated using transmission electron microscopy (TEM). Figure 1a reveals that thin layers of g-C_3N_4 wrap V_2O_5 nanoparticles.

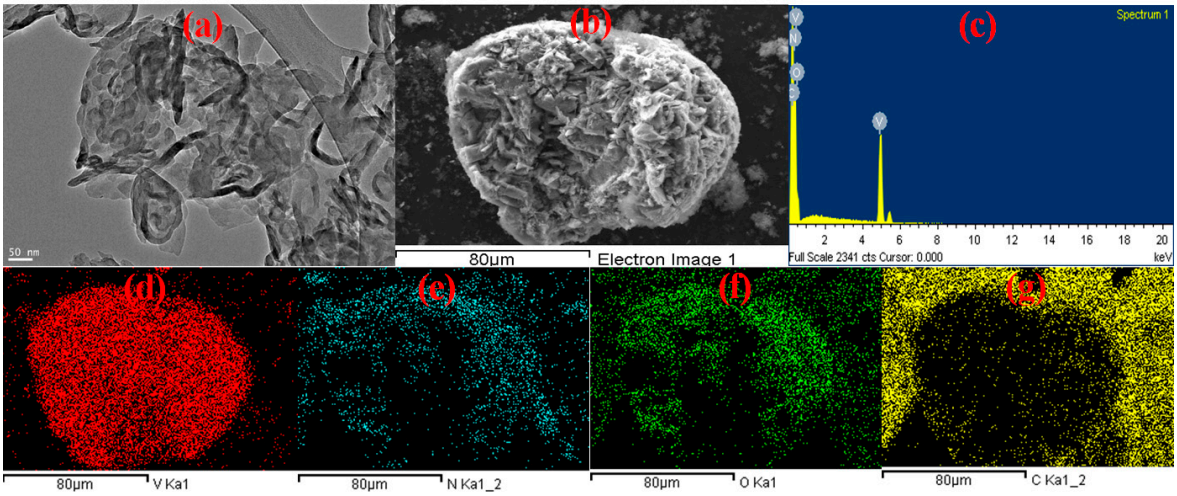

Figure 1. (**a**) TEM image, (**b**) SEM image, (**c**) EDX, and (**d**–**g**) elemental mapping of the V_2O_5-g-C_3N_4 nanosorbent.

Figure 1d–g display the energy dispersive X-ray spectrometer (EDS) maps of the elements V, N, O, and C. EDS maps illustrate the interface between V_2O_5 and carbon nitride. It is clearly seen that the components are dispersed uniformly, this result confirmed the successful combination of these nanomaterials.

The XRD technique was utilized to investigate the produced materials' structure, purity, and phase composition. Figure 2a displays the XRD patterns of the as-fabricated V_2O_5, g-C_3N_4, and the V_2O_5-g-C_3N_4 nanosorbent. The two distinctive diffraction peaks at 12.9° and 27.4° are attributed to the (100) and (002) planes of g-C_3N_4, respectively. In addition, the orthorhombic crystal structure of V_2O_5 is shown by the prominent diffraction peaks at $2\theta = 34.08°, 31.07°, 26.19°, 20.31°$, and 15.42° corresponding to the (310), (301), (110), (001), and (200) planes (JCPDS 41–1426) [43]. Both the definite diffraction peaks of g-C_3N_4

and the orthorhombic phase of V_2O_5 are observable in XRD patterns of V_2O_5-g-C_3N_4, and no other impurities are detected, confirming the purity of the fabricated nanocomposites. Figure 2b depicts the N_2 adsorption-desorption isotherms of the V_2O_5-g-C_3N_4 nanosorbent as manufactured. The isotherms are type IV, confirming the mesoporous structure of the V_2O_5-g-C_3N_4 nanocomposites. The V_2O_5-g-C_3N_4 surface area is 61.04 m^2/g. Thus, the nanocomposites featured a greater surface area and additional active sites, favoring adsorption efficiency.

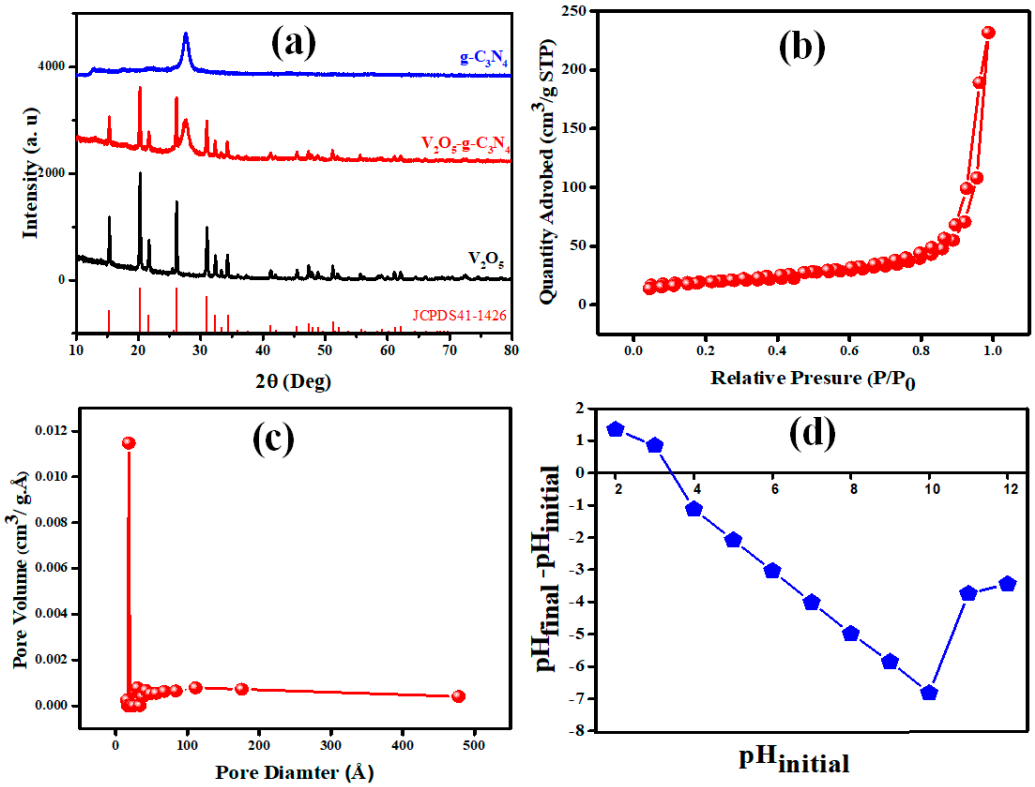

Figure 2. (**a**) XRD patterns of V_2O_5-g-C_3N_4, V_2O_5, and g-C_3N_4, (**b**) nitrogen adsorption–desorption isotherm, (**c**) pore size distribution, and (**d**) plot for the determination of pHZPC for the V_2O_5-g-C_3N_4 nanosorbent.

The graph of point zero charges (Figure 2d) was generated by plotting the difference between the beginning and final pH against the initial pH. The V_2O_5-g-C_3N_4's point zero charges (pzc) were 3.83. The surface of the V_2O_5-g-C_3N_4 nanosorbent is positively charged when the pH is less than pzc and negatively charged when the pH is higher than pzc.

X-ray photoelectron spectra (XPS) were used to examine the surface chemical compositions of the V_2O_5-g-C_3N_4 nanosorbent. The XPS spectra of the V_2O_5-g-C_3N_4, depicted in Figure 3a, demonstrate that the nanosorbent consisted of vanadium, oxygen, nitrogen, and carbon. Figure 3b displays the XPS spectra of C1s. The presence of two characteristic peaks at 285.2 and 281.9 eV can be deduced from the data in Figure 3b, attributed to the carbon sp^2 (C=N-) and carbon sp^3 hybridization (C-C) [44]. Figure 3c shows the XPS spectra of N1s. Two characteristic peaks were found at 395.7 and 397.4 eV, attributed to the nitrogen sp^2 (-C=N-) and sp^3 hybridization (-N-C), respectively [45]. Figure 3d depicts the XPS spectra of O1s, in which the distinctive peak of the oxygen atom in V_2O_5 was shown to have a binding energy of 527.4 eV [46]. The V2p's XPS spectral (Figure 3e) highlights the presence of two peaks at 527.9 and 514.7 eV, which correspond to $V2p_{1/2}$ and $V2p_{3/2}$, respectively.

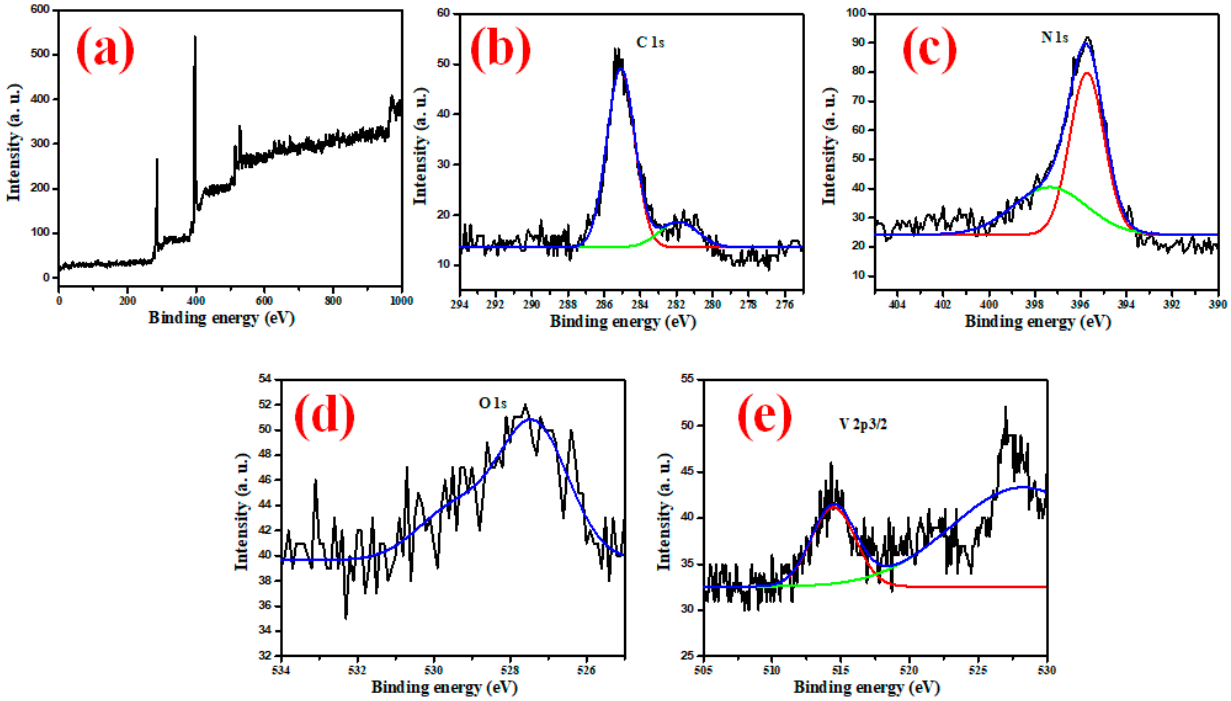

Figure 3. (**a**) XPS spectrum of the V_2O_5-g-C_3N_4 nanosorbent, and XPS spectra survey of (**b**) C 1s, (**c**) N 1s, (**d**) O1s and (**e**) V 2p3/2 for the V_2O_5-g-C_3N_4 nanosorbent.

2.2. Dyes Adsorption onto the V_2O_5-g-C_3N_4 Nanocomposite

2.2.1. Adsorption Capability of the V_2O_5-g-C_3N_4 Nanocomposite towards Organic Dyes

The V_2O_5-g-C_3N_4 nanocomposite was tested with various organic dye solutions for constant concentrations equal to 50 ppm. Experiments on dye removal were conducted under magnetic stirring by combining 10 mg of the V_2O_5-g-C_3N_4 nanocomposite with 25 mL of the dye's aqueous solution for 24 h (Figure 4a). The ability of the V_2O_5-g-C_3N_4 nanocomposite to absorb various dyes from an aqueous solution was evaluated. Figure 4b depicts the percentage of elimination of various dyes by the V_2O_5-g-C_3N_4 nanocomposite. Results confirmed that the removal ability percentages of BF, MG, CV, CR, and MO were 94%, 76.8%, 98.9%, 94.4%, and 5.4%, respectively. This result suggests that the V_2O_5-g-C_3N_4 nanocomposite is an efficient sorbent for eliminating CV, MG, BF, and CR dyes from wastewater.

2.2.2. Impact of Initial pH and Concentration on CV Dyes Elimination

Monitoring the effectiveness of nanoadsorbents in wastewater treatment relies heavily on pH levels [1,47]. The fluctuations in pH lead to modifications in the surface characteristics of the adsorbent and the degree of ionization of adsorptive molecules [2,48]. As is evident from Figure 4c, pH fluctuations significantly impact the percentage of CV dye removed from a solution. With an initial CV concentration of 50 ppm and a nanoadsorbent dosage of 10 mg, the effect of pH was investigated in the range between 2 and 12. Figure 4b demonstrates that as the pH of the solution reached 7, the CV dye removal percentage achieved its greatest values. The V_2O_5-g-C_3N_4 nanocomposite revealed removal percentages of 15, 62, 99, 85, and 77% for CV dye at pH 2, 4, 7, 9, and 12, respectively. The V_2O_5-g-C_3N_4 nanocomposite surface was positively charged at lower pH, resulting in electrostatic repulsion with the cationic CV dye molecules and, as a result, a decreased adsorption efficiency. Wathukarage et al. showed that woody biochar interacts electrostatically with CV molecules at a pH higher than pzc, whereas the biochar surface covered with positive charges below pzc develops electrostatic repulsion with the cationic CV molecules [49].

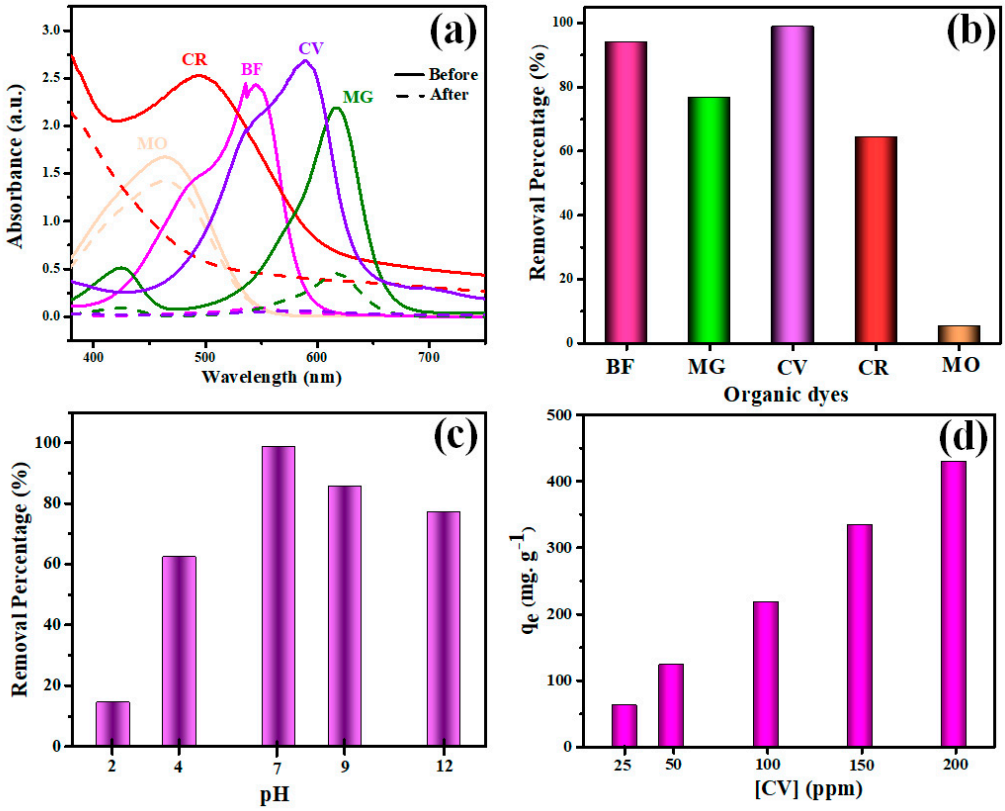

Figure 4. (**a**) UV−Vis curves for various organic dye solutions before and after adsorption, (**b**) adsorption ability, (**c**) pH effect, and (**d**) concentration impact on CV removal by the V_2O_5-g-C_3N_4 nanocomposite.

The influence of CV dye concentration on the amount adsorbed was also studied. The investigations were carried out with 20 mg of the V_2O_5-g-C_3N_4 nanocomposite at a pH value equal to 7. The CV adsorption capacity increased dramatically from 62.9 to 429.6 mg g^{-1} when the concentration of CV dye was raised from 25 to 200 ppm, as seen in Figure 4d. Increasing the CV's initial concentration furnished an effective driving force to overcome all resistance to the migration of CV molecules from the aqueous solution [47].

2.2.3. Adsorption Isotherms Modeling

The adsorption result for CV dye was based on widely analyzed adsorption isotherm models (Langmuir and Freundlich) to estimate the maximum adsorption capacity presented by the V_2O_5-g-C_3N_4 *nanocomposite* for CV dye. The Langmuir model depicts chemical adsorption and implies that the adsorption process occurs on a homogeneous monolayer surface with comparable adsorption energy requirements for all active sites [50]. The Freundlich model describes physical adsorption and assumes it occurs on a multilayer heterogeneous surface with different adsorption sites and variable affinities [50]. Table 1 presents the nonlinear formulas for the used isotherms. The results of nonlinear isotherm graphs for CV adsorption onto V_2O_5-g-C_3N_4 are shown in Figure 5a, and the estimated isotherm parameters are listed in Table 1.

Table 1. Equilibrium isotherm constants models for CV dye adsorption by the V_2O_5-g-C_3N_4 nanosorbent.

Equilibrium Model	Non-Linear Form	Parameters	Values
Langmuir [51]	$q_e = \frac{q_{max} K_L\ C_e}{1+K_L\ C_e}$	q_m (mg g^{-1})	664.65
		K_L (mg g^{-1})	0.058
		R_L (L. mg^{-1})	0.08
		R^2	0.995
Freundlich [52]	$q_e = k_F C_e^{1/2}$	n	2.33
		K_F (L. mg^{-1})	73.25
		R^2	0.974

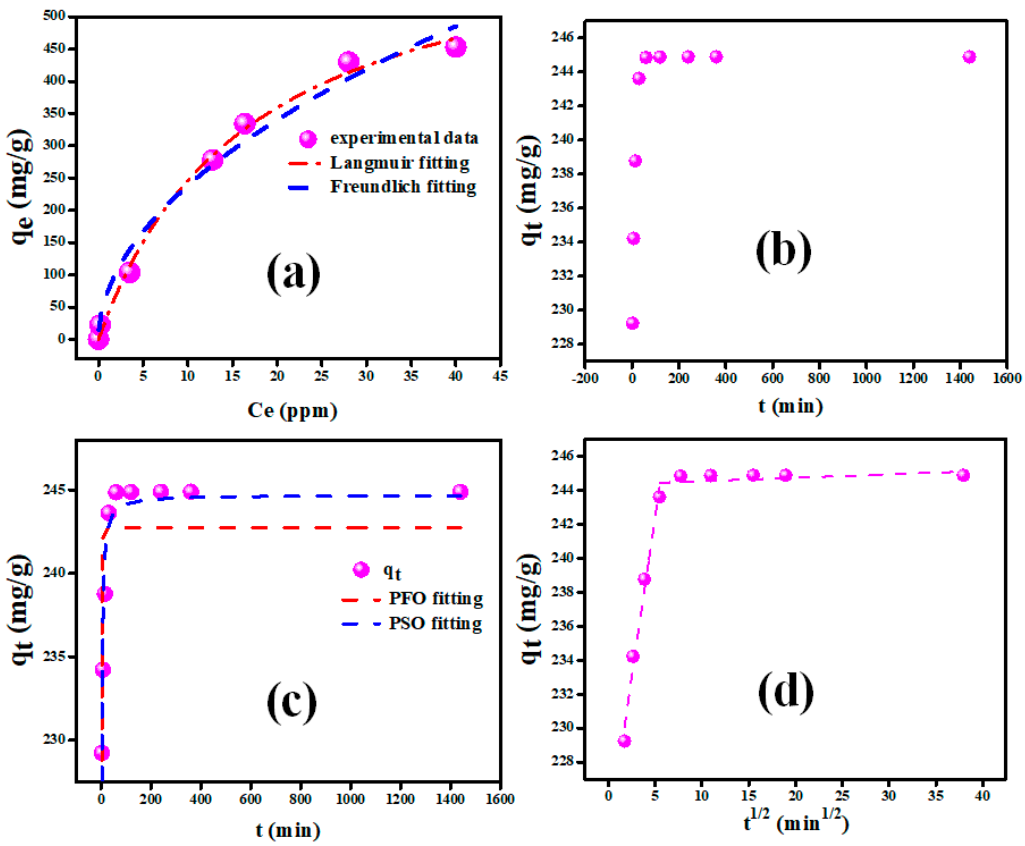

Figure 5. (**a**) Adsorption isotherms modeling, (**b**) contact time effect, (**c**) adsorption kinetics modeling, and (**d**) intraparticle diffusion of CV adsorption onto the V_2O_5-g-C_3N_4 nanocomposite.

The correlation coefficient (R^2) for the fitted plot of the Langmuir isotherm is 0.995, which is greater than the R^2 for the Freundlich isotherm (0.974). This result indicates that the Langmuir model is well-fitted, indicating the monolayer adsorption of CV molecules on the V_2O_5-g-C_3N_4 nanocomposite. Following the Langmuir model, it was established that the maximum adsorption capacity of V_2O_5-g-C_3N_4 was 664.65 mg/g. In addition, the equilibrium parameter R_L ($= \frac{1}{1+K_L.C_0}$) was used to determine whether or not the adsorption was favorable. The R_L value was found to be 0.08, which was in the 0–1 range, affirming that the adsorption was favorable. The capacity of V_2O_5-g-C_3N_4 nanocomposite to adsorb CV dye has been compared to several adsorbents mentioned in the literature (Table 2).

Table 2. Observation of CV adsorption capacities of the V_2O_5-g-C_3N_4 nanocomposite with the different nanomaterials' adsorbents.

Adsorbents	q_e (mg g^{-1})	pH	References
Xanthated Rice husks	90.02	10	[53]
Saccharum munja biomass-functionalized carbon nanotubes	180.51	7	[54]
Nascent Rice Husk	24.47	10	[55]
Cellulose based on sugarcane	107.50	8–13	[56]
Nocardiopsis sp	15.90	7	[57]
MChs-Ppy	11.84	8	[58]
GO@NPANI@$ZrSiO_4$	15.81	7	[59]
Fe noparticles/βCD	100	9	[60]
V_2O_5-g-C_3N_4 *nanocomposite*	664.65	7	This paper

2.2.4. Contact Time and Adsorption Kinetics Modeling

In order to establish the optimal time required for the maximal uptake of CV dye by the V_2O_5-g-C_3N_4 nanocomposite, the impact of contact time on the CV adsorption was investigated for various contact times ranging from 3 to 1440 min at 25 °C. The effects of contact time on the adsorption process are illustrated in Figure 5b. The adsorption capabilities of the V_2O_5-g-C_3N_4 nanocomposite grew rapidly during the first 20 min and reached equilibrium, with no significant changes after that. At the start of the process, the adsorption rate was very fast due to the availability of many active sites on the surface of the V_2O_5-g-C_3N_4 nanocomposite. As a result, the concentration of the remaining active sites decreased at equilibrium, and the sorption rate decreased dramatically. As a result, beyond this optimum value, the elimination of CV molecules remained unaltered.

For the optimal selection of the adsorption kinetics model, CV adsorption over the V_2O_5-g-C_3N_4 nanocomposite at a concentration of 100 ppm CV was investigated. The pseudo-first order (PFO) and pseudo-second order (PSO) plotting graphs were presented in Figure 5c by plotting q_t against time. The parameters of adsorption kinetics denoted by k_1, k_2, q_e, and R^2 of the evaluation model were determined theoretically using nonlinear fitting and are reported in Table 3. The R^2 values indicated that CV adsorption on the V_2O_5-g-C_3N_4 nanocomposite is well-defined using the PSO model, which agrees with the experimental result.

Table 3. Kinetics models for CV adsorption by the V_2O_5-g-C_3N_4 nanocomposite.

Kinetics Models	Equations	Parameters	Values
PFO [61]	$q_t = -\left(1 - e^{-1k_1 t}\right)$	q_e (mg g^{-1}) k_1 (min^{-1}) R^2	242.71 0.95 0.606
PSO [61]	$q_t = \frac{t\ k_2 q_e^2}{k_2 q_e t + 1}$	$q_{e(\text{calculated})}$ (mg g^{-1}) $q_{e(\text{experimental})}$ (mg g^{-1}) k_2 (g mg^{-1}·min^{-1}) R^2	244.69 0.018 0.932
IPD [62]	$q_t = k_{dif}\sqrt{t} + C$	C_1 (mg g^{-1}) K_{dif1} (mg g^{-1} min$^{1/2}$) R^2 C_2 (mg g^{-1}) K_{dif2} (mg g^{-1} min$^{1/2}$) R^2	223.53 3.77 0.983 244.35 0.02 0.908

Weber's intraparticle diffusion was used to fit the experimental data in order to comprehend the adsorption kinetics and rate-controlling stages better. The intraparticle diffusion model is chosen as the application model by graphing q_t against $t_{1/2}$. Figure 5d

depicts the intraparticle diffusion process curves of CV adsorbed over the V_2O_5-g-C_3N_4 nanocomposite. The adsorption procedure consists of two steps. The initial stage is film diffusion, wherein CV molecules diffuse from the solution to the outer surface of the V_2O_5-g-C_3N_4 nanocomposite. The intraparticle diffusion stage is the second step, and is influenced by the surface morphology as well as the number of void sites that are present in the V_2O_5-g-C_3N_4 nanocomposite. K_{dif1} was considerably greater than K_{dif2}, indicating that the intraparticle diffusion phase was a smooth process [63]. The intercept at the second step was larger than that at the first step, which indicates a greater contribution of surface adsorption in the step that controls the rate [64]. In addition, the R^2 values in the two phases were, respectively, 0.983 and 0.908, which indicates that Weber's intraparticle diffusion model had great application in investigating the CV adsorption mechanism.

2.2.5. Adsorption Mechanism

The mechanism of CV dye adsorption onto the V_2O_5-g-C_3N_4 nanocomposite may imply electrostatic interactions, physical adsorption, π–π interactions, and hydrogen bonds [65,66]. To comprehend the adsorption process, the FTIR spectra of V_2O_5-g-C_3N_4 before and after CV dye adsorption were recorded in the range of cm^{-1} (Figure 6a). Hydrogen bonding may have a significant role in CV dye adsorption. The broadband between 3000 and 3500 cm^{-1}, attributed to the O–H and terminal amino group stretching modes, slightly shifted, revealing the embroilment of the OH and amino groups of the nanocomposite in the adsorption process. As a result, the existence of hydrogen bonds between CV dyes and V_2O_5-g-C_3N_4 can be confirmed. The π–π interactions represent an essential mechanism between the π-electrons in organic molecules with aromatic rings and those in a carbon nitride substance, according to several investigations that have validated this phenomenon [67]. The vibrational triazine ring mode at 883 cm^{-1} was shifted after CV dye adsorption, and this confirmed the π-π interaction between the aromatic rings of CV molecules and the π-electron clouds of V_2O_5-g-C_3N_4. Figure 6b depicts the possible CV adsorption mechanism onto the V_2O_5-g-C_3N_4 nanocomposite.

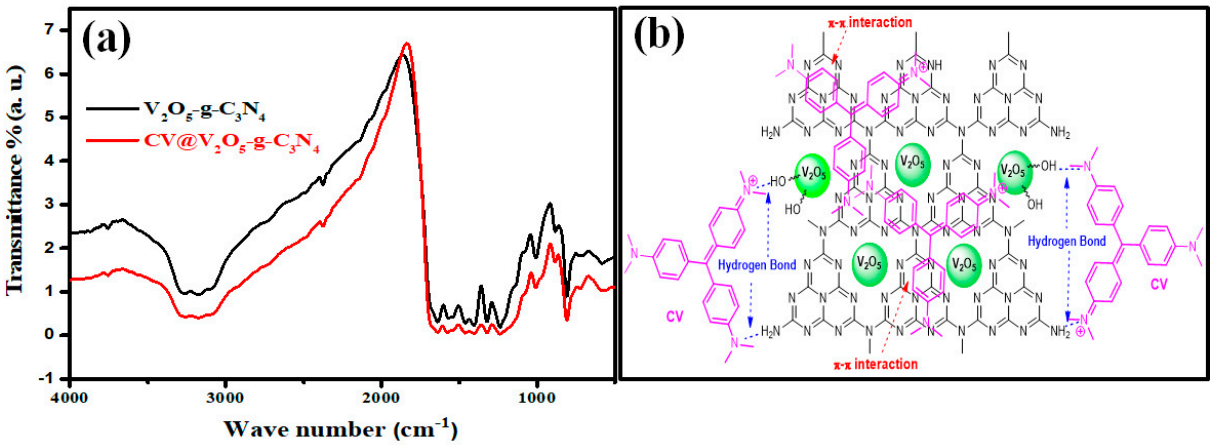

Figure 6. (**a**) FTIR spectra of CV@V_2O_5-g-C_3N_4 and (**b**) proposed adsorption mechanism of CV onto V_2O_5-g-C_3N_4.

2.2.6. Reusability Test

Along with having a high adsorption capacity, an ideal adsorbent should also have high reusability, as this would help to keep the overall cost of the adsorption process to a minimum. The reusability tests for the V_2O_5-g-C_3N_4 *nanocomposite* for the removal of CV dye was conducted four times with the same adsorbent dose, as shown in Figure 7. Following the adsorption experiment, the previously utilized V_2O_5-g-C_3N_4 *nanocomposites* were first recovered using filtering and then calcined at a temperature of 500 degrees Celsius for one hour. Following that, the obtained V_2O_5-g-C_3N_4 was utilized again. As a result of the reusability performance trial, depicted in Figure 7, it is possible to notice that

V_2O_5-g-C_3N_4 can perform the CV elimination process effectively for at least four cycles, with a mean value of around 92%.

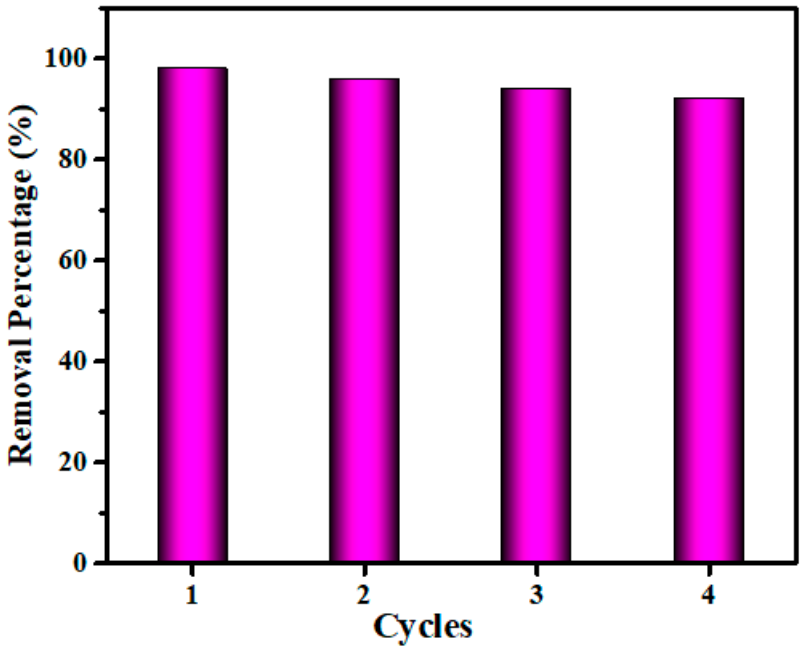

Figure 7. Reusability efficiency of the V_2O_5-g-C_3N_4 nanocomposite.

3. Materials and Methods

3.1. Chemicals

Ammonium vanadate ($NH_4VO_3 \geq 99.0\%$), urea ($\geq$98.0%), crystal violet (CV $\geq$ 90%), malachite green (MG $\geq$ 90%), basic fuchsin (BF $\geq$ 85%), Congo red (CR $\geq$ 97.0%), methyl orange (MO $\geq$ 98%), sodium hydroxide (NaOH $\geq$ 99%), sodium chloride (NaCl $\geq$ 99%), and hydrochloric acid (HCl $\geq$ 37%) purchased from Merck Company were used without further purification. The required CV concentrations (25 to 200 ppm) were obtained by diluting CV stock solution (500 ppm).

3.2. Nanomaterials Synthesis

V_2O_5 nanomaterials were fabricated by thermal decomposition of ammonium vanadate (NH_4VO_3) at 400 °C for 2 h in the air atmosphere. The g-C_3N_4 nanostructures were generated by the thermal polymerization approach [68]. In the typical method, 4000 mg of urea powder was calcined at 550 °C in an alumina crucible with a cap in an electric furnace at a heating rate of 4.6 °C/min for 120 min. A yellowish solid powder was formed after cooling to ambient temperature through natural means.

For the V_2O_5-g-C_3N_4 nanocomposite fabrication, 800 mg of solid g-C_3N_4 powder was distributed in 115 mL of ethanol and sonicated for 30 min. After adding 1800 mg of V_2O_5 nanoparticles, the mixed solution was rapidly agitated for 60 min. The suspension was then heated at 75 degrees Celsius for 24 h to evaporate the organic solvent. The resultant solid was then annealed at 150 °C for 120 min to generate the V_2O_5-g-C_3N_4 nanocomposite.

3.3. The V_2O_5-g-C_3N_4 Nanocomposite Characterization

Employing JEOL, JEM-2100 transmission electron microscopy (TEM), the production and distribution of the V_2O_5-g-C_3N_4 nanocomposite were investigated. The nanocomposite morphology was investigated by JEOL, JEM-6700F field emission scanning electron microscopy (FESEM). Energy dispersive X-ray spectrometer (EDS) analysis was performed to determine the notional stoichiometry composition of nonmaterial surfaces. The crystallinity grade and phase construction were scrutinized through X-ray diffraction (XRD) using a Bruker D8–Advance equipped with a Cu-K source (λ = 0.15418 nm). The porosity and BET

surface area were measured using N_2 adsorption-desorption at 77 K and a Micromeritics 2010 device. Using FTIR (Nicolet 6700) in the 4000–400 cm^{-1} range with a resolution of 4 cm^{-1}, the chemical bonding and stretching vibration of the produced samples before and after CV dye adsorption were analyzed.

3.4. CV Dye Adsorption Procedure

Batch removal studies were conducted by contacting 20 mg of the V_2O_5-g-C_3N_4 nanocomposite sorbent with 50 mL of CV dye solution at varying starting concentrations (25–200 mg/L). In 50 mL screw-top bottles, the mixture was swirled on a magnetic stirrer at 400 rpm for 24 h, which was longer than necessary to achieve equilibrium. A comparison with other organic dyes (malachite green (MG), basic fuchsin (BF), Congo red (CR), and methyl orange (MO)) was also performed by dissolving 20 mg of the V_2O_5-g-C_3N_4 nanocomposite in 50 mL of dye solution (50 ppm) and magnetically stirring for 24 h. After each experiment, the solutions were centrifuged and the residual dye concentrations were measured with a SHIMADZU UV-1650PC spectrophotometer. The residual dye concentrations were determined at a maximum wavelength of 590 nm for CV, 617 nm for MG, 545 nm for BF, 497 nm for CR, and 467 nm for MO. Then, the concentration of dyes was obtained, and equilibrium dye capacity (q_e (mg g^{-1})) was calculated using the following equation:

$$q_e = \frac{V(C_0 - C_e)}{m}$$

where m is the mass of the adsorbent (g), V is the volume of the solution (L), and C_0 and C_e (mg L^{-1}) are the dye concentrations at time equal to 0 and equilibrium, respectively.

For the kinetic experiment, the volume and initial concentration of dyes were 150 mL and 250 ppm, respectively, while the mass of the V_2O_5-g-C_3N_4 nanocomposite was 60 mg. The test was conducted in the dark while magnetic stirring was taking place. Later, 5 mL of the suspension was withdrawn and centrifuged at predetermined intervals to determine the remaining CV dye concentration. The following equation was employed to determine the adsorbed quantity q_t (mg g^{-1}) at time t:

$$q_t = \frac{V(C_0 - C_t)}{m}$$

The Origin 2016b program was used to plot and model the experimental data.

4. Conclusions

The V_2O_5-g-C_3N_4 nanocomposite with a greater surface area was successfully synthesized using the sonication method. The study findings demonstrated a good CV dye removal efficiency. The evaluation of V_2O_5-g-C_3N_4 as a possible adsorbent for various dyes (BF, MG, CV, CR, and MO), demonstrated the overall high potential of the nanocomposite for the removal of dyes from wastewaters. In order to improve V_2O_5-g-C_3N_4's effectiveness in removing CV dye, an investigation into the influence of pH was carried out. The removal of CV dye by the V_2O_5-g-C_3N_4 nanocomposite was found to be pH-dependent. The greatest adsorption capacity for CV pollutants was found at a pH of 7, 664.65 mg g^{-1}. Several kinetic and adsorption models were utilized in this study to evaluate the removal of CV by V_2O_5-g-C_3N_4. The PSO kinetics and the Langmuir adsorption isotherm models were found to fit the data best. According to the FTIR analysis results, the CV adsorption mechanism was connected to π–π interactions and the hydrogen bond.

Author Contributions: The study design, preparation of materials, data collection, and analysis were contributed by all authors. Each author provided feedback on prior drafts of the article. The final manuscript was read and approved by all authors. All authors have read and agreed to the published version of the manuscript.

Funding: The authors extend their appreciation to the Deputyship for Research & Innovation, Ministry of Education, Saudi Arabia for funding this research work through the project number (QU-IF-4-5-1–31384).

Data Availability Statement: Not applicable.

Acknowledgments: The authors extend their appreciation to the Deputyship for Research & Innovation, Ministry of Education, Saudi Arabia for funding this research work through the project number (QU-IF-4-5-1–31384). The authors also thank to Qassim University for technical support.

Conflicts of Interest: We declare that we do not have any commercial or associative interest that could potentially influence or bias the submitted work.

References

1. Aissa, B.; Khezami, L.; Taha, K.; Elamin, N.; Mustafa, B.; Al-Ayed, A.; Modwi, A. Yttrium oxide-doped ZnO for effective adsorption of basic fuchsin dye: Equilibrium, kinetics, and mechanism studies. *Int. J. Environ. Sci. Technol.* **2021**, *19*, 9901–9914. [CrossRef]
2. Rahali, S.; Ben Aissa, M.A.; Khezami, L.; Elamin, N.; Seydou, M.; Modwi, A. Adsorption behavior of Congo red onto barium-doped ZnO nanoparticles: Correlation between experimental results and DFT calculations. *Langmuir* **2021**, *37*, 7285–7294. [CrossRef] [PubMed]
3. Adam, F.A.; Ghoniem, M.; Diawara, M.; Rahali, S.; Abdulkhair, B.Y.; Elamin, M.; Aissa, M.A.B.; Seydou, M. Enhanced adsorptive removal of indigo carmine dye by bismuth oxide doped MgO based adsorbents from aqueous solution: Equilibrium, kinetic and computational studies. *RSC Adv.* **2022**, *12*, 24786–24803. [CrossRef] [PubMed]
4. Li, J.; Xiong, Y.; Wan, H.; Chen, J.; Fang, S.; Song, X.; Li, R.; Duan, M.; Hu, R. In-situ investigation of dye pollutant adsorption performance on graphitic carbon nitride surface: ATR spectroscopy experiment and MD simulation insight. *J. Hazard. Mater.* **2021**, *418*, 126297. [CrossRef]
5. Largo, F.; Haounati, R.; Ouachtak, H.; Hafid, N.; Jada, A.; Addi, A.A. Design of organically modified sepiolite and its use as adsorbent for hazardous Malachite Green dye removal from water. *Water Air Soil Pollut.* **2023**, *234*, 183. [CrossRef]
6. Ouachtak, H.; Akhouairi, S.; Addi, A.A.; Akbour, R.A.; Jada, A.; Douch, J.; Hamdani, M. Mobility and retention of phenolic acids through a goethite-coated quartz sand column. *Colloids Surf. A Physicochem. Eng. Asp.* **2018**, *546*, 9–19. [CrossRef]
7. Alizadeh, N.; Shariati, S.; Besharati, N. Adsorption of crystal violet and methylene blue on azolla and fig leaves modified with magnetite iron oxide nanoparticles. *Int. J. Environ. Res.* **2017**, *11*, 197–206. [CrossRef]
8. Ouachtak, H.; El Guerdaoui, A.; El Haouti, R.; Haounati, R.; Ighnih, H.; Toubi, Y.; Alakhras, F.; Rehman, R.; Hafid, N.; Addi, A.A. Combined molecular dynamics simulations and experimental studies of the removal of cationic dyes on the eco-friendly adsorbent of activated carbon decorated montmorillonite Mt@AC. *RSC Adv.* **2023**, *13*, 5027–5044. [CrossRef]
9. Pathak, A.; Khandegar, V.; Kumar, A. Statistical Investigation in Conjunction with a Box–Behnken Design for the Removal of Dyes Using Electrocoagulation. *J. Hazard. Toxic Radioact. Waste* **2022**, *26*, 04022001. [CrossRef]
10. Kyi, P.P.; Quansah, J.O.; Lee, C.-G.; Moon, J.-K.; Park, S.-J. The removal of crystal violet from textile wastewater using palm kernel shell-derived biochar. *Appl. Sci.* **2020**, *10*, 2251. [CrossRef]
11. Nguyen, T.A.; Juang, R.-S. Treatment of waters and wastewaters containing sulfur dyes: A review. *Chem. Eng. J.* **2013**, *219*, 109–117. [CrossRef]
12. Chakraborty, S.; Chowdhury, S.; Saha, P.D. Adsorption of crystal violet from aqueous solution onto NaOH-modified rice husk. *Carbohydr. Polym.* **2011**, *86*, 1533–1541. [CrossRef]
13. Thekkedath, A.; Sugaraj, S.; Sridharan, K. Nanomaterials in Advanced Oxidation Processes (AOPs) in Anionic Dye Removal. In *Advanced Oxidation Processes in Dye-Containing Wastewater*; Springer: Berlin/Heidelberg, Germany, 2022; pp. 129–165.
14. Varjani, S.; Rakholiya, P.; Shindhal, T.; Shah, A.V.; Ngo, H.H. Trends in dye industry effluent treatment and recovery of value added products. *J. Water Process Eng.* **2021**, *39*, 101734. [CrossRef]
15. Ali, H.; Muhammad, S.K. Biosorption of crystal violet from water on leaf biomass of Calotropis procera. *J. Environ. Sci. Technol* **2008**, *1*, 143–150. [CrossRef]
16. Lin, J.; Pan, Z.; Wang, X. Photochemical reduction of CO2 by graphitic carbon nitride polymers. *ACS Sustain. Chem. Eng.* **2014**, *2*, 353–358. [CrossRef]
17. Yang, W.; Godin, R.; Kasap, H.; Moss, B.; Dong, Y.; Hillman, S.A.; Steier, L.; Reisner, E.; Durrant, J.R. Electron accumulation induces efficiency bottleneck for hydrogen production in carbon nitride photocatalysts. *J. Am. Chem. Soc.* **2019**, *141*, 11219–11229. [CrossRef] [PubMed]
18. Xie, K.; Fang, J.; Li, L.; Deng, J.; Chen, F. Progress of graphite carbon nitride with different dimensions in the photocatalytic degradation of dyes: A review. *J. Alloys Compd.* **2022**, *901*, 163589. [CrossRef]
19. Toghan, A.; Modwi, A. Boosting unprecedented indigo carmine dye photodegradation via mesoporous MgO@g-C3N4 nanocomposite. *J. Photochem. Photobiol. A Chem.* **2021**, *419*, 113467. [CrossRef]

20. Shvalagin, V.V.; Korzhak, G.V.; Kuchmiy, S.Y.; Skoryk, M.A.; Selyshchev, O.V.; Zahn, D.R. Facile preparation and high photocatalytic activity of crystalline graphitic carbon nitride in hydrogen evolution from electron donor solutions under visible light. *J. Photochem. Photobiol. A Chem.* **2020**, *390*, 112295. [CrossRef]
21. Yan, L.; Gao, H.; Chen, Y. Na-Doped Graphitic Carbon Nitride for Removal of Aqueous Contaminants via Adsorption and Photodegradation. *ACS Appl. Nano Mater.* **2021**, *4*, 7746–7757. [CrossRef]
22. Ding, P.; Ji, H.; Li, P.; Liu, Q.; Wu, Y.; Guo, M.; Zhou, Z.; Gao, S.; Xu, W.; Liu, W. Visible-light degradation of antibiotics catalyzed by titania/zirconia/graphitic carbon nitride ternary nanocomposites: A combined experimental and theoretical study. *Appl. Catal. B Environ.* **2022**, *300*, 120633. [CrossRef]
23. Zhu, Y.; Cai, W.; Zhao, Y.; Mu, X.; Zhou, X.; Chu, F.; Wang, B.; Hu, Y. Graphite-like Carbon Nitride/Polyphosphoramide Nanohybrids for Enhancement on Thermal Stability and Flame Retardancy of Thermoplastic Polyurethane Elastomers. *ACS Appl. Polym. Mater.* **2022**, *4*, 121–128. [CrossRef]
24. Yang, J.; Wang, H.; Jiang, L.; Yu, H.; Zhao, Y.; Chen, H.; Yuan, X.; Liang, J.; Li, H.; Wu, Z. Defective polymeric carbon nitride: Fabrications, photocatalytic applications and perspectives. *Chem. Eng. J.* **2022**, *427*, 130991. [CrossRef]
25. Alaghmandfard, A.; Ghandi, K. A Comprehensive Review of Graphitic Carbon Nitride (g-C_3N_4)–Metal Oxide-Based Nanocomposites: Potential for Photocatalysis and Sensing. *Nanomaterials* **2022**, *12*, 294. [CrossRef]
26. Khezami, L.; Aissa, M.A.B.; Modwi, A.; Ismail, M.; Guesmi, A.; Algethami, F.K.; Ticha, M.B.; Assadi, A.A.; Nguyen-Tri, P. Harmonizing the photocatalytic activity of g-C3N4 nanosheets by ZrO_2 stuffing: From fabrication to experimental study for the wastewater treatment. *Biochem. Eng. J.* **2022**, *182*, 108411. [CrossRef]
27. Fernandes, E.; Drosopoulou, S.; Mazierski, P.; Miodyńska, M.; Gołaszewska, D.; Zaleska-Medynska, A.; Martins, R.C.; Gomes, J. Carbon nitride photoactivation evaluation and degradation of a mixture of parabens by ozone assistance. *J. Water Process Eng.* **2022**, *49*, 103018. [CrossRef]
28. Falletta, E.; Longhi, M.; Di Michele, A.; Boffito, D.C.; Bianchi, C.L. Floatable graphitic carbon nitride/alginate beads for the photodegradation of organic pollutants under solar light irradiation. *J. Clean. Prod.* **2022**, *371*, 133641. [CrossRef]
29. Wang, T.; Huang, M.; Liu, X.; Zhang, Z.; Liu, Y.; Tang, W.; Bao, S.; Fang, T. Facile one-step hydrothermal synthesis of α-Fe_2O_3/gC_3N_4 composites for the synergistic adsorption and photodegradation of dyes. *RSC Adv.* **2019**, *9*, 29109–29119. [CrossRef]
30. Liu, G.; Qiao, X.; Gondal, M.; Liu, Y.; Shen, K.; Xu, Q. Comparative study of pure g-C_3N_4 and sulfur-doped g-C_3N_4 catalyst performance in photo-degradation of persistent pollutant under visible light. *J. Nanosci. Nanotechnol.* **2018**, *18*, 4142–4154. [CrossRef]
31. Wang, A.; Wang, C.; Fu, L.; Wong-Ng, W.; Lan, Y. Recent advances of graphitic carbon nitride-based structures and applications in catalyst, sensing, imaging, and LEDs. *Nano-Micro Lett.* **2017**, *9*, 47. [CrossRef]
32. Dong, J.; Zhang, Y.; Hussain, M.I.; Zhou, W.; Chen, Y.; Wang, L.-N. g-C_3N_4: Properties, Pore Modifications, and Photocatalytic Applications. *Nanomaterials* **2021**, *12*, 121. [CrossRef]
33. Modwi, A.; Khezami, L.; Ghoniem, M.; Nguyen-Tri, P.; Baaloudj, O.; Guesmi, A.; AlGethami, F.; Amer, M.; Assadi, A. Superior removal of dyes by mesoporous MgO/g-C_3N_4 fabricated through ultrasound method: Adsorption mechanism and process modeling. *Environ. Res.* **2022**, *205*, 112543. [CrossRef]
34. Toghan, A.; Abd El-Lateef, H.M.; Taha, K.K.; Modwi, A. Mesoporous TiO_2@g-C_3N_4 composite: Construction, characterization, and boosting indigo carmine dye destruction. *Diam. Relat. Mater.* **2021**, *118*, 108491. [CrossRef]
35. Modwi, A.; Ismail, M.; Idriss, H.; Aissa, M.; Khezami, L.; Bououdina, M. Efficient Removal of Cd (II) from Aquatic Media by Heteronanostructure MgO@TiO_2@g-C_3N_4. *J. Nanomater.* **2022**, *2022*, 1458442. [CrossRef]
36. Mirhosseini, H.; Shamspur, T.; Mostafavi, A. Novel adsorbent g-C_3N_4/ZnV_2O_4 for efficient removal of crystal violet dye: Removal process optimization, adsorption isotherms, and kinetic modeling. *Appl. Organomet. Chem.* **2022**, *36*, e6867. [CrossRef]
37. Wei, S.; Kamali, A.R. Waste plastic derived Co_3Fe_7/$CoFe_2O_4$@carbon magnetic nanostructures for efficient dye adsorption. *J. Alloys Compd.* **2021**, *886*, 161201. [CrossRef]
38. Wei, S.; Kamali, A.R. Trifunctional mesoporous magnetic adsorbent-photocatalyst nanocomposite for efficient removal of potassium ethyl xanthate from mining wastewater. *J. Water Process Eng.* **2022**, *49*, 103067. [CrossRef]
39. Modwi, A.; Idriss, H.; Khezami, L.; Albadri, A.; Ismail, M.; Assadi, A.A.; Nguyen-Tri, P. Ba^{2+} removal from aquatic medium via TiY2O5@g-C3N4 nanocomposites. *Diam. Relat. Mater.* **2023**, *135*, 109830. [CrossRef]
40. Zang, Y.-N.; Yang, S.-S.; Ding, J.; Zhao, S.-Y.; Chen, C.-X.; He, L.; Ren, N.-Q. A biochar-promoted V_2O_5/gC_3N_4 Z-Scheme heterostructure for enhanced simulated solar light-driven photocatalytic activity. *RSC Adv.* **2021**, *11*, 15106–15117. [CrossRef]
41. Sajid, M.M.; Shad, N.A.; Javed, Y.; Khan, S.B.; Zhang, Z.; Amin, N.; Zhai, H. Preparation and characterization of Vanadium pentoxide (V_2O_5) for photocatalytic degradation of monoazo and diazo dyes. *Surf. Interfaces* **2020**, *19*, 100502. [CrossRef]
42. Ali, H.; Ismail, A. Honeycomb-like V_2O_5 based films: Synthesis, structural, thermal, and optical properties for environmental applications. *J. Inorg. Organomet. Polym. Mater.* **2022**, *32*, 3012–3029. [CrossRef]
43. Chen, H.; Chen, L.; Meng, J.; Yang, Z.; Wu, J.; Rong, Y.; Deng, L.; Shi, Y. Synergistic effects in V_3O_7/V_2O_5 composite material for high capacity and long cycling life aqueous rechargeable zinc ion batteries. *J. Power Sources* **2020**, *474*, 228569. [CrossRef]
44. Gao, Y.; Zhu, Y.; Lyu, L.; Zeng, Q.; Xing, X.; Hu, C. Electronic structure modulation of graphitic carbon nitride by oxygen doping for enhanced catalytic degradation of organic pollutants through peroxymonosulfate activation. *Environ. Sci. Technol.* **2018**, *52*, 14371–14380. [CrossRef]

45. Wang, H.; Yuan, X.; Wu, Y.; Zeng, G.; Chen, X.; Leng, L.; Li, H. Synthesis and applications of novel graphitic carbon nitride/metal-organic frameworks mesoporous photocatalyst for dyes removal. *Appl. Catal. B Environ.* **2015**, *174*, 445–454. [CrossRef]
46. Zhang, X.; Jia, X.; Duan, P.; Xia, R.; Zhang, N.; Cheng, B.; Wang, Z.; Zhang, Y. V2O5/Pg-C3N4 Z-scheme enhanced heterogeneous photocatalytic removal of methyl orange from water under visible light irradiation. *Colloids Surf. A Physicochem. Eng. Asp.* **2021**, *608*, 125580. [CrossRef]
47. Khezami, L.; Aissa, M.A.B.; Modwi, A.; Guesmi, A.; Algethami, F.K.; Bououdina, M. Efficient removal of organic dyes by Cr-doped ZnO nanoparticles. *Biomass Convers. Biorefinery* **2022**, 1–14. [CrossRef]
48. Ghoniem, M.G.; Ali, F.A.M.; Abdulkhair, B.Y.; Elamin, M.R.A.; Alqahtani, A.M.; Rahali, S.; Ben Aissa, M.A. Highly selective removal of cationic dyes from wastewater by MgO nanorods. *Nanomaterials* **2022**, *12*, 1023. [CrossRef]
49. Wathukarage, A.; Herath, I.; Iqbal, M.; Vithanage, M. Mechanistic understanding of crystal violet dye sorption by woody biochar: Implications for wastewater treatment. *Environ. Geochem. Health* **2019**, *41*, 1647–1661. [CrossRef]
50. Kalam, S.; Abu-Khamsin, S.A.; Kamal, M.S.; Patil, S. Surfactant adsorption isotherms: A review. *ACS Omega* **2021**, *6*, 32342–32348. [CrossRef]
51. Al-Ghouti, M.A.; Razavi, M.M. Water reuse: Brackish water desalination using Prosopis juliflora. *Environ. Technol. Innov.* **2020**, *17*, 100614. [CrossRef]
52. Ayawei, N.; Ebelegi, A.N.; Wankasi, D. Modelling and interpretation of adsorption isotherms. *J. Chem.* **2017**, *2017*, 3039817. [CrossRef]
53. Homagai, P.L.; Poudel, R.; Poudel, S.; Bhattarai, A. Adsorption and removal of crystal violet dye from aqueous solution by modified rice husk. *Heliyon* **2022**, *8*, e09261. [CrossRef] [PubMed]
54. Yadav, A.; Bagotia, N.; Yadav, S.; Sharma, N.; Sharma, A.K.; Kumar, S. Environmental application of Saccharum munja biomass-derived hybrid composite for the simultaneous removal of cationic and anionic dyes and remediation of dye polluted water: A step towards pilot-scale studies. *Colloids Surf. A Physicochem. Eng. Asp.* **2022**, *650*, 129539. [CrossRef]
55. Quansah, J.O.; Hlaing, T.; Lyonga, F.N.; Kyi, P.P.; Hong, S.-H.; Lee, C.-G.; Park, S.-J. Nascent rice husk as an adsorbent for removing cationic dyes from textile wastewater. *Appl. Sci.* **2020**, *10*, 3437. [CrossRef]
56. El Naeem, G.A.; Abd-Elhamid, A.; Farahat, O.O.; El-Bardan, A.A.; Soliman, H.M.; Nayl, A. Adsorption of crystal violet and methylene blue dyes using a cellulose-based adsorbent from sugercane bagasse: Characterization, kinetic and isotherm studies. *J. Mater. Res. Technol.* **2022**, *19*, 3241–3254.
57. Adenan, N.H.; Lim, Y.Y.; Ting, A.S.Y. Nocardiopsis sp. for the removal of triphenylmethane dyes: Decolorization and optimization studies. *Water Air Soil Pollut.* **2021**, *232*, 414. [CrossRef]
58. Mashkoor, F.; Nasar, A. Facile synthesis of polypyrrole decorated chitosan-based magsorbent: Characterizations, performance, and applications in removing cationic and anionic dyes from aqueous medium. *Int. J. Biol. Macromol.* **2020**, *161*, 88–100. [CrossRef]
59. Mahmoud, M.E.; Amira, M.F.; Seleim, S.M.; Nabil, G.M.; Abouelanwar, M.E. Multifunctionalized graphene oxide@nanopolyaniline@zirconium silicate nanocomposite for rapid microwable removal of dyes. *J. Nanostruct. Chem.* **2021**, *11*, 645–662. [CrossRef]
60. Nasiri, J.; Motamedi, E.; Naghavi, M.R.; Ghafoori, M. Removal of crystal violet from water using β-cyclodextrin functionalized biogenic zero-valent iron nanoadsorbents synthesized via aqueous root extracts of Ferula persica. *J. Hazard. Mater.* **2019**, *367*, 325–338. [CrossRef]
61. Lagergren, S.K. About the theory of so-called adsorption of soluble substances. *Sven. Vetenskapsakad. Handingarl* **1898**, *24*, 1–39.
62. Chien, S.; Clayton, W. Application of Elovich equation to the kinetics of phosphate release and sorption in soils. *Soil Sci. Soc. Am. J.* **1980**, *44*, 265–268. [CrossRef]
63. Alatalo, S.-M.; Mäkilä, E.; Repo, E.; Heinonen, M.; Salonen, J.; Kukk, E.; Sillanpää, M.; Titirici, M.-M. Meso-and microporous soft templated hydrothermal carbons for dye removal from water. *Green Chem.* **2016**, *18*, 1137–1146. [CrossRef]
64. Cheng, J.; Zhan, C.; Wu, J.; Cui, Z.; Si, J.; Wang, Q.; Peng, X.; Turng, L.-S. Highly efficient removal of methylene blue dye from an aqueous solution using cellulose acetate nanofibrous membranes modified by polydopamine. *ACS Omega* **2020**, *5*, 5389–5400. [CrossRef] [PubMed]
65. Liu, D.; Gu, W.; Zhou, L.; Wang, L.; Zhang, J.; Liu, Y.; Lei, J. Recent advances in MOF-derived carbon-based nanomaterials for environmental applications in adsorption and catalytic degradation. *Chem. Eng. J.* **2022**, *427*, 131503. [CrossRef]
66. Sun, W.; Liu, T.; Xia, K.; Zhou, J.; Liu, X.; Zhang, X. Preparation of Adsorbent Based on Polyacrylate Latex Solid Waste and Its Application in the Treatment of Dye Wastewater. *ACS Omega* **2022**, *7*, 13243–13253. [CrossRef]
67. Gupta, K.; Khatri, O.P. Reduced graphene oxide as an effective adsorbent for removal of malachite green dye: Plausible adsorption pathways. *J. Colloid Interface Sci.* **2017**, *501*, 11–21. [CrossRef]
68. Ali, M.; Modwi, A.; Idriss, H.; Aldaghri, O.; Ismail, M.; Ibnaouf, K. Detoxification of Pb (II) from aquatic media via $CaMgO_2$@g-C_3N_4 nanocomposite. *Mater. Lett.* **2022**, *322*, 132501. [CrossRef]